Trajectory of a Model Bacterium

Akanksha Thawani† and Mahesh S. Tirumkudulu‡

Department of Chemical Engineering, Indian Institute of Technology Bombay, Powai, Mumbai 400076. India.

(Received ?; revised ?; accepted ?. - To be entered by editorial office)

It is well known that bacteria, such as *Escherichia coli*, propel themselves in aqueous media by rotating helically shaped flagella. While a number of theoretical approaches have been proposed to model the detailed swimming motion, a rigorous comparison with experimental data is lacking due to the difficulty in simultaneously visualizing the motion of the head and the flagella along with the resulting trajectory. To this end, we have built a macroscopic working model of a bacterium and visualized its detailed motion in high viscosity liquid. We show that small asymmetry in the mass distribution in the head can lead to helical trajectories with large pitch and radius, which are reminiscent of the wiggling trajectories observed for swimming bacteria. The detailed motion agrees well with the predictions from slender body theory that accounts for the asymmetric mass distribution in the head. Our study shows that the trajectory consists of two helical trajectories of different length scales - a large one caused by the asymmetric mass distribution and set by the head rotation rate and a smaller one caused by the rotating flagellum and set by its rotation rate. We discuss implications of these results on the wiggling trajectories of swimming bacteria.

Key words:

1. Introduction

Bacteria such as *Escherichia coli* or *Bacillus subtilis*, propel themselves in suspending liquids using slender filamentous projections known as flagella, which are powered by rotating motors at their base. When all the motors turn in the same direction, the flagella bundle together to form a rotating helix, which propels the cell forward. This swimming motion is called a run (Berg 2004). When one or more motors reverse their direction, the corresponding flagella come apart from the bundle resulting in an abrupt change in the direction of the cell with resulting motion termed as a tumble. The motion of a flagellated bacterium is a series of runs interspersed by tumbles (Berg 2004).

Given the small physical dimension of the bacterium $\sim O(1\ \mu\text{m})$ and their swimming speeds of $O(10\ \mu\text{m}/s)$ in aqueous environments, the fluid flow generated by the moving bacterium is governed by low Reynolds number hydrodynamics, $Re \lesssim O(10^{-4})$. The propulsion generated by rotating helical flagella originates from the difference in the drag experienced by a slender body when moved along its axis compared to its broadside, latter being approximately twice compared to when the rod is moved along its axis. Thus, when a section of the slender helical flagellum rotates such that the velocity vector of the segment has components along both the segment and its perpendicular direction, the force vector is not aligned along the velocity vector and has a

† Department of Chemical and Biological Engineering, Princeton University, Princeton NJ, USA
‡ Email address for correspondence: mahesh@che.iitb.ac.in

non-zero component along the axis of the helix (Chwang & Wu 1971). The sum of this force component from all segments of the helix gives the total thrust exerted by the rotating flagella. Since the cell including its head and flagella experience no external force, the thrust is balanced by the drag on the moving head under steady motion. Similarly, the torque generated due to the rapid rotation of flagella ($\sim$ 100 Hz for *E. coli*) is balanced by a counter-rotating head ($\sim$ 10 Hz for *E. coli*) so that the net torque on the cell is zero.

Keller & Rubinow (1976) (henceforth referred to as KR) were the first to investigate theoretically the detailed motion of a bacterium and relate it to the geometry and dynamics of the rotating flagellum. They adopted the resistive-force theory (RFT) of Gray & Hancock (1955), where the force and torque on a flagellum is obtained by integrating the local forces on each infinitesimal segment. After adding the drag force and torque on the spherical head and applying the force-free and torque-free conditions, the resulting velocity components yield a helical trajectory. However, the RFT theory ignores the hydrodynamic interactions between different parts of the flagella and also between the head and the flagella, leading to significant errors when the wavenumber (or turns) of the helical flagellum is large (Rodenborn *et al.* 2013). A more accurate approach of slender-body theory pioneered by Lighthill (1976), Hancock (1953), Johnson (1980) and Higdon (1979) involves distributing stokeslets and dipoles of suitable strength along the centerline of the flagellum so as to match the boundary condition on the flagellum surface. A known velocity distribution along the flagellum, yields the strength of stokeslets and dipoles, and therefore the total force and torque exerted by the rotating flagellum. A third approach is to numerically solve the full three-dimensional Stokes equation using the boundary element method (Phan-Thien *et al.* 1980), the regularized flow singularity method (Cortez 2001; Cortez *et al.* 2005), or the immersed boundary method (Dillon *et al.* 2001). For details on the various approaches, the reader is referred to reviews on bacterial hydrodynamics by Lauga & Powers (2009) and Lauga (2016).

While a number of theoretical studies have focused on determining the details of bacterial motion, a rigorous comparison with the experimental data has been largely missing. It is only recently that a study measured thrust, drag and torque for a rotating (model) flagellum and compared the measurements with theoretical predictions (Rodenborn *et al.* 2013) but it still does not give insight into the resulting swimming trajectory of a bacterium. The main reason for the limited experiments on bacterial motion lies with the constraints of the visualization technique. The head and the flagella are typically labeled with a fluorescent dye and visualized with a high numerical aperture objective lens. Consequently, even a small out-of-plane motion of cells renders them out of focus within a short time due to which long-time reliable data on trajectories with simultaneous visualization of head and flagella becomes difficult. In addition, variations in the geometry and dimensions of flagella and cell body in a population lead to variations in head and flagellar rotation rates (Darnton *et al.* 2007), as well as the resulting trajectories.

~~The aforementioned aspects are highlighted in the~~ A recent study by Hyon *et al.* (2012) ~~who measured~~ visualized trajectories of *Bacillus subtilis* and found large variation in the pitch and the radius of these trajectories. The experiments did not measure the rotation speeds of ~~the head and the tail . The~~ head and tail but the trajectories were compared with predictions obtained via simulations that employed the method of regularized stokeslets using boundary element analysis. Their model considered ~~a single flagellum~~ both a single bundle and multiple bundles of flagella attached to an ellipsoidal head, either aligned along the major axis of the ellipsoid or off-axis at some fixed angles. ~~The predicted radius and pitch of the trajectory were much smaller than the measurements when the helical flagellum was aligned along the major axis of the head. Further, the model under-predicts the measured pitch even when an~~ They found good match with their measurements for the case of multiple flagella, rotating off-axis ~~flagellum is considered. They attribute the differences between the prediction and the measurements mainly to the presence of multiple off-axis flagellabundles in the head, which when accounted for led to wiggling trajectories closer to the measurements. While the presence of multiple off-axis flagella~~

~~reported previously in an experimental study was the motivation for the extensive calculations, a~~ with the head. However, an absence of simultaneous visualization of the ~~multiple off-axis~~ flagella, head and ~~the resulting wiggle would be needed for~~ swimming trajectory prevented a detailed comparison ~~of the predictions with the experiments~~with model predictions.

To overcome the aforementioned drawbacks, we built a macroscopic model of a bacterium, henceforth referred to as a *bot* constituting a spherical head and a single helical flagellum whose motion was visualized accurately in a tank containing high viscosity liquid. While the current study was motivated by that of Hyon *et al.* (2012) to better understand the wiggling trajectories in real bacteria, the experiments were inspired by GI Taylor's illustration of bacterial motion using a mechanized bot swimming in a very viscous liquid (Taylor 1967) and his study on motion of a macroscopic model of spermatozoan (Taylor 1952). Our experiments involved visualization of not only the detailed dynamics of the flagellum and the head but also the entire trajectory of the bot. Thus the goal of our experiments was to measure simultaneously the trajectory, and the rotation rate of the helix (flagellum) and the head and compare the measurements with the predictions of the slender-body theory. The measurements ~~should not only reveal~~ reveal not only intricacies of bacterial swimming such as the possible cause for wiggling trajectories observed in real bacteria but also act as benchmarks for future theoretical studies, especially those for collective motion of bacteria, wherein error estimates for the various theoretical models of a single swimmer can be ascertained.

2. Material and Methods

2.1. *Experimental set-up*

The experiments were performed in a 70L-tank (36.5 cm x 34 cm x 50 cm high) filled up to a height of about 43.5 cm with silicone oil (Wacker®) of dynamic viscosity of 0.97 Pa-s (25°C). The tank dimensions and the area of interest for the run were chosen such that the head is away from the side walls by about 15 cm, and the free surface (top) by about 20 cm. The viscosity measurements were performed with a cone and plate rheometer (Anton Paar MCR-301) and found to be in close agreement with the estimates provided by the manufacturer. The fluid was mixed thoroughly to avoid temperature variation or density stratification in the tank, and the experiments were started after ensuring that the convection currents and bubbles generated during mixing were eliminated.

A hollow, plastic sphere of external diameter 37 mm and shell thickness of 2 mm was used to construct the head of the model bacterium (Fig. 1). The head contained a small motor (M1N10FB95G of 5 V rated voltage, a no-load current of 20 mA, and starting torque of 1.8 mN.m), a pair of batteries (3 V, CR2450 or 3 V, CR2032) and wire terminals to connect the motor to the battery. The size and specification of the batteries were selected to overcome the volume limitations inside the spherical head, net-weight restrictions ~~of the model~~ for a neutrally buoyant bot and battery capacity required to sustain high torque in the viscous fluid. The plastic sphere was cut into two halves and the motor along with the batteries were fit into one half with the rotor protruding out of a small hole at the center of the hemisphere surface. Double-sided tape was used to stick the motor to both the hemisphere and the batteries. The wires connecting the motor and the battery were passed through a small hole at the center of the other hemisphere's surface but the connections were left open so that the motor could be switched on and off after the hemispheres were sealed. The length of the protruding wires was kept to a minimum (about 4-5 mm) to minimize its drag and therefore its influence on the overall trajectory.

In order to balance the weight of the model bacterium, metallic and plastic rings were glued around the stator, such that the weight is symmetrically distributed about the axis of the stator. Despite taking extreme care, small asymmetry in the weight distribution led to a small tilt of the

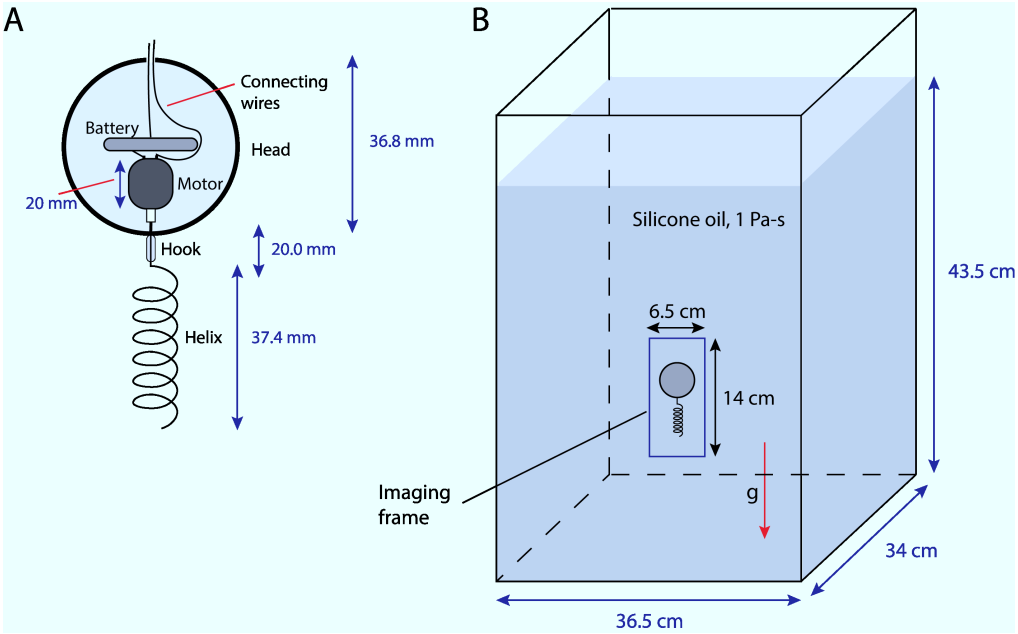

FIGURE 1. (A) A schematic of the model bacterium used in the experiments. (B) Dimensions of the tank and the approximate location of the bot during a run.

bot, about 8° with respect to the vertical. As will be discussed later, the small tilt contributes significantly to the overall motion of the bot. The small gap between the protruding rotor and the thin wall of the hemisphere was closed with thick grease to prevent silicone oil from entering the spherical head. The rotor was connected to a metallic helix (flagellum) through a connecting plastic tube, similar to the bacterial hook. The model flagellum was constructed from an initially straight copper wire and the wire was wrapped around brass mandrels with helical grooves to obtain the helix. Note that the flagellum (made of metal) is *heavier* than the surrounding fluid, and thus the head was made *lighter* in order for the entire body to be of the same density as the fluid. Consequently, the bot was stable in the vertical position while swimming from the bottom of the tank to the top (see Fig. 1(B)). The bot was released at the bottom of the tank and at equal distance from the left and right side walls and the trajectory was recorded only when the bot was in the middle of the tank, using a high speed CCD camera (Pike F-032 CCD; see Movie S1). The physical parameters of the bot and the surrounding fluid are listed in Table 1.

2.2. *Trajectories*

Image analysis revealed the trajectory of the center of the spherical head and the rotation rate of the head and the helix. The position of the head was obtained using a MATLAB code that identifies the center of the sphere in each frame. The rotation rate of the head and the helix, however, were obtained manually using reference points marked on the bot.

The images of the bot at three different time instants are presented in Fig. 2(A). The bot precessed about the vertical coordinate (Y axis) due to the tilt. The horizontal dashed line connecting the images highlights the translation of the bot as a function of time. The coordinates of a typical trajectory are presented in Fig. 2(B). The slight tilt of the bot with the vertical leads to a considerable wobble in the trajectory. The camera, however, can only capture the projection of the motion on to the XY plane (gravity acts in the negative Y direction). There is an initial transient when the bot is released at the bottom of the tank but the trajectory reaches a steady state within a short time. We observed a large wobble with pitch and diameter of 8.8 mm and 2.8

Length of helix	L	37.5 mm
Number of turns	N_λ	6
Wavenumber	$k = 2\pi/\lambda = 2\pi N_\lambda/L$	1 mm^{-1}
Radius of helix	R	2.7 mm
Radius of helix wire	a	0.62 mm
Radius of head	b	18.4 mm
Length of hook	h	20.0 mm
Buoyancy-balanced weight difference between the head and the flagellum	δm	0.9 g
Tilt with gravity	α	7.6°
Rotation rate of helix	ω_{wave}	37.7 rad/s
Density of fluid	ρ	960 kg/m^3
Viscosity of fluid	μ	0.97 Pa-s

TABLE 1. Parameters for the experimental bot used for predicting the trajectory.

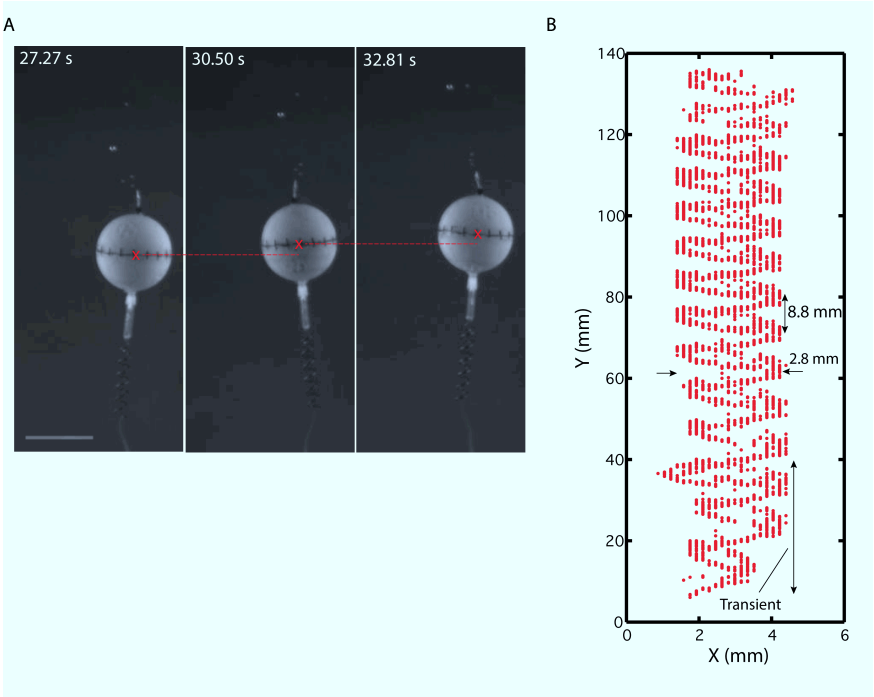

FIGURE 2. (A) Snapshots of the swimming bot at three different times. The symbol "x" ~~in red~~ marks the center of the head while the horizontal dashed line highlights the displacement of the bot. Scale bar, 28.2 mm. (B) Trajectory extracted from image analysis. Note that there is an initial transient at the start of the experiment during which both the pitch and the radius of the bot varies. The pitch and radius of the helical trajectory is found to be 8.8 mm and 1.4 mm, respectively. See Movie S1. See also supplementary section VI.

mm, respectively, where the wobble dimensions are of the same order of magnitude as the bot itself. Interestingly, this has also been observed in the trajectory measurements of *Bacillus subtilis* Hyon *et al.* (2012). The large wobble was reproducible across different, independent experimental runs using the same bot as well as multiple constructions of the bot with similar dimensions (Section VI, Supplementary Materials).

The wobble is assumed to be similar in the Z direction as in X, but the position would appear

sinusoidally shifted in time by half a wavelength due to the difference in the projections of the three-dimensional trajectory on the YZ and the YX planes. Further, the velocity component along Y is found to decrease gradually with time, due to the slow discharge of the batteries driving the model bacterium. Thus, the apparent helical rotation rate of the flagellum, along with head counter-rotation rate, is observed to decrease with time too (see discussion pertaining to Fig. 3).

2.3. *Benchmark studies*

In the experiment discussed above, the Reynolds number calculated with respect to the flagellar rotation, $Re_f \equiv \rho\omega_{wave}R^2/\mu$ is of $O(0.1)$ and that with respect to head translation is $Re_h \equiv \rho Ub/\mu \sim O(0.01)$. Here, ρ and μ are the density and the viscosity of the liquid, R is the radius of the helix, ω_{wave} is the rotation rate of the helix, b is the radius of the spherical head, and U is the characteristic translation velocity of the bot. In order to test the applicability of low Reynolds number hydrodynamics in the observed range of Reynolds numbers, we performed two benchmark tests. The first consisted of a rotating helix which was soldered to the shaft of a motor and the force generated was measured using a weighing scale. An externally-powered motor was used to drive the helical flagellum at varying rotation rate and the generated thrust was found to be in agreement with predictions from the slender body theory, similar to the previous study of Rodenborn *et al.* (2013). The second test consisted of sedimentation of a sphere of dimensions identical to the spherical head wherein the weight of the sphere was adjusted such that the buoyancy resulted in a velocity similar to the translational velocity of the bot. The measurements were then compared with the prediction obtained using the Stokes equation. The propulsive force observed in the first test showed a maximum of 15% error compared to theoretical values, which is of the same magnitude as the errors observed by Rodenborn *et al.* (2013), and the sedimentation velocities were found to closely agree with the theoretical predictions of Stokes flow (within 7%). The results and analysis are included in sections II and III of Supplementary Materials.

2.4. *Calculations using Slender-body theory*

The calculation of the velocity and the angular rotation of the head and the helix follow the procedure detailed by Lighthill (1976) and Higdon (1979). We built up on the MATLAB code generously shared by Rodenborn *et al.* (2013). The head of the bot is a sphere while the flagellum is a rigid right-handed helix rotating with helical wave velocity ω_{wave} radians per second relative to the head (Fig. 3(A)). The coordinate frame has its origin at the head center and is henceforth referred to as the body frame. The rotation in clockwise direction as seen from behind the flagellum, i.e. $\omega_{wave} < 0$ in our coordinate system, results in propulsion in the negative z-direction. To balance the torque, the body counter-rotates at $\mathbf{\Omega_H}$ rad/s, leading to an apparent rotation of the helix in the local body frame at $\mathbf{\Omega}$ rad/s. Note that $\mathbf{\Omega_H} = \mathbf{\Omega} - (0, 0, \omega_{wave})$.

The force distribution on the surrounding fluid due to the motile bacterium is determined by distributing stokeslets and doublets on the flagellum to satisfy the boundary conditions in velocity. The propelling flagellum is approximated by a slender body with each point being represented as a combination of a stokeslet and a doublet. By imposing appropriate velocity boundary conditions, the distribution of the stokeslets and doublets can be determined and thus the force exerted by the body on the fluid. Here, we follow the approximation suggested by Lighthill (1976) along with certain corrections due to the presence of the spherical head by Higdon (1979). We present only a brief description of the method and the reader is referred to Higdon (1979) and Rodenborn *et al.* (2013) for details. Lighthill (1976) showed that if stokeslets of magnitude $\mathbf{f}(s)$ per unit length are placed along the length of the helix, which is equal to the force per unit length exerted by the helix on the surrounding fluid, then doublets of strength $\frac{-a^2\mathbf{f}_\perp(s)}{4\mu}$ per unit length are required to satisfy the no-slip boundary condition on the surface of the flagellum. Here, s is the arc length along the centerline of the flagellum from some fixed point on the centerline and $\mathbf{f}_\perp(s)$ is the projection of $\mathbf{f}(s)$ perpendicular to the centerline of the flagellum.

The local velocity of a segment of the flagellum located at s_0 is related to the force distribution along the flagella,

$$\mathbf{u}_s(s_0) = \frac{\mathbf{f}_\perp(s_0)}{4\pi\mu} + \int_{|r_0(s,s_0)|>\delta} \frac{r_0^2\mathbf{f}(s) + (\mathbf{f}(s).\mathbf{r_0})\mathbf{r_0}}{8\pi\mu r_0^3}\mathrm{d}s, \tag{2.1}$$

where, $\mathbf{r_0}$ is the position vector of the point s_0 on the centerline of the flagellum relative to the point s, $\delta = a\sqrt{e}/2 = 0.82a$ is the natural cutoff length and e is the base of natural logarithm. The flagellum is attached to the head at the point $(0, 0, b)$ such that the position of any point beyond the straight hook of length h on the centerline of the flagellum ($z > b + h$; Fig. 3A) is given by,

$$\mathbf{r} = (R\cos(k(z-b-h)), R\sin(k(z-b-h)), z)\,.$$

Note that the stokeslets in (2.1) represent the velocity field generated by point forces in an infinite medium but for the present case the flow field does not satisfy the no-slip condition on the surface of the head. Higdon (1979) corrected for this by replacing the stokeslet with Green's function that consisted of the stokeslet plus a collection of image singularities that ensure the no-slip boundary condition on the head's surface. In the present calculation, this correction is ignored leading to a small error (discussed later).

In addition to the disturbance flow generated by the moving flagellum, the moving head also contributes to the velocity at the location of the flagellum, which is given by

$$\mathbf{u}_H(\mathbf{r}) = \frac{3}{4}b\left[\left(\frac{\mathbb{I}}{r} + \frac{\mathbf{rr}}{r^3}\right) - \frac{b^2}{3}\left(-\frac{\mathbb{I}}{r^3} + \frac{3\mathbf{rr}}{r^5}\right)\right].\mathbf{U} + \frac{b^3}{r^3}\mathbf{r}\times\mathbf{\Omega_H}, \tag{2.2}$$

where $\mathbf{r}$ is the position vector of a segment of the flagellum with respect to the center of the head. The first term in square bracket represents the contribution from the stokeslet and dipole due to translation of the spherical head, and the last term represents the contribution of the rotlet due to the rotation of the head. Thus the velocity of the centerline of a segment is given by the sum of the velocity contribution from the moving head and that from the fluid flow generated by rest of the flagellum,

$$\mathbf{u_f}(\mathbf{r}) = \mathbf{u}_s(\mathbf{r}) + \mathbf{u}_H(\mathbf{r}) = \mathbf{U} + \mathbf{\Omega}\times\mathbf{r}, \tag{2.3}$$

where $\mathbf{u_f}(\mathbf{r})$ is the velocity of the particular segment located at $\mathbf{r}$, $\mathbf{U}$ is the translational velocity of the body and $\mathbf{\Omega}$ is the apparent rotation rate of the flagellum in the body frame.

Equation (2.1-2.3) can be used to obtain the force distribution on the flagellum for a fixed velocity of the flagellum. A short summary of the discretization procedure and the numerical implementation is presented here and the reader is referred to Rodenborn *et al.* (2013) for details. The grid size was chosen to be larger than the cutoff length and the discretized equation (2.1), say for the i^{th} node ($i = 1...M$), was divided into two parts. The first is an integral from δ to the grid size while the other is the velocity contribution of the stokeslets located on other nodes. The discretized equation (2.1-2.3) is solved in the local coordinates of each discretized point for the local forces $\mathbf{f}'_i$. The force at each discretized node is then converted back into the body frame via a coordinate transformation ($\mathbf{f}'_i \rightarrow \mathbf{f}_i$) as suggested by Rodenborn *et al.* (2013). The discretized form of equation (2.1-2.3) in the body frame becomes,

$$\begin{pmatrix}\mathbf{u}_1\\ \mathbf{u}_2\\ \vdots\\ \mathbf{u}_M\end{pmatrix} = \mathbb{P}\begin{pmatrix}\mathbf{f}_1\\ \mathbf{f}_2\\ \vdots\\ \mathbf{f}_M\end{pmatrix} + \begin{pmatrix}\mathbf{q}_1\\ \mathbf{q}_2\\ \vdots\\ \mathbf{q}_M\end{pmatrix}$$

where $\mathbf{q}_i \forall i \in \{1, M\}$ depend on of the geometry of the flagellum and input value of ω_{wave}. The

torque contribution of each stokeslet acting on the flagellum is given by, $\mathbf{t}_i = \mathbf{r} \times \mathbf{f}_i$. The disturbance flow caused by a stokeslet $\mathbf{f}_i$ on the flagellum also exerts a force on the spherical head (Higdon 1979), so that the total force contribution of the stokeslets on the bacterium (head plus flagellum) is given by,

$$\mathbf{f}_i(1 + C_T) + \frac{(\mathbf{f_i} \cdot \mathbf{r})\mathbf{r}}{r^2}(C_R - C_T) \tag{2.4}$$

where,

$$C_R = -\frac{3}{2}\frac{b}{r} + \frac{1}{2}\frac{b^3}{r^3}, \quad \text{and} \quad C_T = -\frac{3}{4}\frac{b}{r} - \frac{1}{4}\frac{b^3}{r^3}.$$

Similarly, the total torque contribution of a stokeslet including that due to the disturbance flow caused at the center of the head is given by,

$$\mathbf{r} \times \mathbf{f}_i \left(1 - \frac{b^3}{r^3}\right). \tag{2.5}$$

Using the discretized form of (2.1) and the total force and the torque contribution of each stokeslet, we obtain a propulsion matrix $\mathbb{G}^h$ for the flagellum,

$$\begin{pmatrix} \mathbf{F}^h \\ L^{-1}\mathbf{T}^h \end{pmatrix} = \mathbb{G}^h \begin{pmatrix} \mathbf{u} \\ L\mathbf{\Omega} \end{pmatrix} + \mathbf{Q} \tag{2.6}$$

where $\mathbf{F}^h$ and $\mathbf{T}^h$ are, respectively, the net propulsion force and net torque exerted by the flagellum. $\mathbf{Q}$ is obtained by propagating the constants $\mathbf{q}_i$ as described above.

Each column of $\mathbb{G}^h$ was determined by keeping the corresponding element of $\mathbf{u}$ or $L\mathbf{\Omega}$ as unity and the rest as null. For example, for the calculation of the third column of the propulsion matrix, $u_z = 1$ i.e., $\mathbf{u}_i$=(0,0,1) $\forall$ i $\in \{1, M\}$. Each $\mathbf{f}_i$ was calculated as described above. The force on each element was then used to determine the discretized torques $\mathbf{t}_i$. The forces and torques are summed up to provide the elements of the propulsion matrix.

So far, the entire calculation is based on the coordinate system local to the body (origin at the center of the head; Fig. 3(A)). While the above calculation will be correct for every instant of time for the flagellum in the local body frame, the position and orientation of the flagellum and head would change with time due to translation and rotation of the entire body, as observed in the laboratory frame (Fig. 2; see next section for detailed description). The calculations of this trajectory in the laboratory frame are greatly simplified if the body frame translates with the center of the head and rotates with the flagellum at every instant of time so that all the equations derived above are valid at all times in this particular body frame of reference. This is similar to the body frame adopted by KR, where their origin is placed at the point connecting the head and the flagellum.

As mentioned previously, the slight asymmetry in the mass distribution inside the head leads to a small tilt in the bot with respect to the vertical. This implies that although the net force on the bot is zero at all times, it experiences an external torque whenever the bot is displaced from its equilibrium tilt position. The external torque due to gravity is given by,

$$\boldsymbol{\ell}'(t) \times \delta m\, \mathbf{g}'(t)\,, \tag{2.7}$$

where $\boldsymbol{\ell}'(t)$ is the vector joining the center of mass of the head to the center of mass of the flagellum, δm is the difference in the mass of the head with that of the fluid displaced by the head, and $\mathbf{g}'(t)$ is the acceleration due to gravity transformed to the body frame (Fig. 3). Therefore, $\boldsymbol{\ell}'(t) = (-\Delta\cos(\omega_{wave}t), -\Delta\sin(\omega_{wave}t), L/2 + b + h)$, where Δ is the distance of the center of mass of the spherical head from the geometric center.

Adding the total force contribution of the stokeslet to the drag force on the head due to translation, $-6\pi\mu b\mathbf{v}$, gives the net force acting on the bot, which is zero. On the other hand, adding the

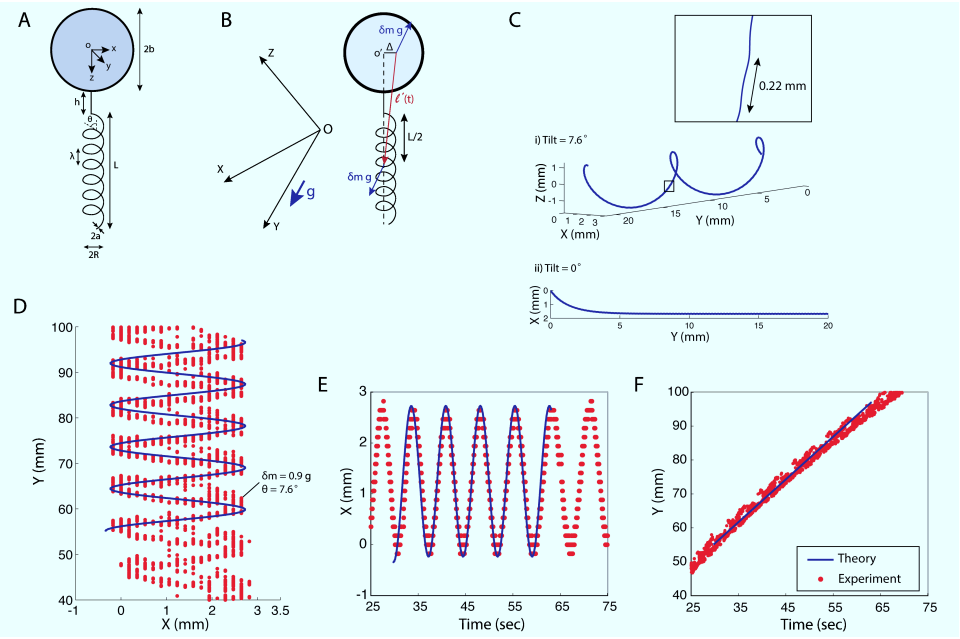

FIGURE 3. (A) Schematic of the model bacterium in the local body frame for the theoretical analysis. (B) Model bacterium (in the laboratory frame) showing the small displacement (Δ) of the center of mass of the spherical head. Since the flagellum is heavier than the fluid by an amount $\delta m\, g$ and the head is lighter by the same amount (so that the entire body is neutrally buoyant), the body experiences a force couple (indicated by the blue arrows) resulting in an equilibrium tilt position with respect to the global coordinates (XYZ). Here, gravity acts in the negative Y direction. (C) Predicted trajectory for the observed tilt angle of 7.6°. The motion of the bot results in a smaller helical motion embedded in a larger helical trajectory, one with a small pitch and radius, and a second larger helical trajectory (wobble). In the absence of tilt, only the former is present. (D) Comparison of the predicted trajectory with measurements. (E-F) The measured time evolution of the position of the center of the head, in X and Y coordinates, is compared with the prediction.

total torque contribution of the stokeslet to the resistive torque of the rotating head, $-8\pi\mu b^3\mathbf{\Omega}_H$, is equal to the external torque due to gravity. Thus the combined force and torque balances become,

$$\begin{pmatrix} -\mathbf{F}^h \\ -L^{-1}\mathbf{T}^h \end{pmatrix} + \begin{pmatrix} -6\pi\mu b\mathbf{v} \\ -8\pi\mu b^3 L^{-1}\mathbf{\Omega}_H \end{pmatrix} + \begin{pmatrix} \mathbf{0} \\ L^{-1}(\boldsymbol{\ell}'(t) \times \delta m\mathbf{g}'(t)) \end{pmatrix} = 0$$

where the expression for $\mathbf{F}^h$ and $L^{-1}\mathbf{T}^h$ are obtained from (2.6). Substituting $\mathbf{\Omega_H} = \mathbf{\Omega} - (0, 0, \omega_{wave})$ gives,

$$-\mathbb{G}^h \begin{pmatrix} \mathbf{v} \\ L\mathbf{\Omega} \end{pmatrix} + \begin{pmatrix} -6\pi\mu b\mathbf{v} \\ -8\pi\mu b^3 L^{-1}\mathbf{\Omega} \end{pmatrix} = \mathbf{Q} + \begin{pmatrix} \mathbf{0} \\ -8\pi\mu b^3 L^{-1}(0, 0, \omega_{wave}) \end{pmatrix} - \begin{pmatrix} \mathbf{0} \\ L^{-1}(\boldsymbol{\ell}'(t) \times \delta m\mathbf{g}'(t)) \end{pmatrix} \quad (2.8)$$

Since the vector $\mathbf{Q}$ depends on ω_{wave} and the geometric parameters, the above set of equations can be solved for $\mathbf{v}$ and $\mathbf{\Omega}$ for a given ω_{wave} and known elements of $\mathbb{G}^h$.

2.5. *Trajectory calculation*

In order to determine the trajectory of the bot, we consider a cartesian coordinate system at rest in the laboratory frame, hereby referred to as $\mathbf{R} = (X, Y, Z)$ (Fig. 3(B)). This requires transformation of the position and orientation of the bot from the body frame to the laboratory frame, $\mathbf{r} \rightarrow \mathbf{R}$. As demonstrated by KR, the transformation from $\mathbf{r}$ to $\mathbf{R}$ consists of a rotation obtained using a transformation matrix $\mathbb{A}^{-1}(t)$, which is a function of time, and a translation by an amount $\mathbf{R_0}(t)$,

the latter being the translation of the center of the head in the laboratory frame. The trajectory of the path is then given by,

$$\mathbf{R}(t) = \mathbf{R_0}(t) + \mathbb{A}^{-1}(t).\mathbf{r}, \tag{2.9}$$

where the second term on the right gives the position of each point on the flagellum with respect to the head center in the laboratory frame. The translation of the center of the head is given by,

$$\frac{d\mathbf{R_0}}{dt} = \mathbb{A}^{-1}(t).\mathbf{v} \tag{2.10}$$

The rotation matrix from body to global frame, $\mathbb{A}^{-1}(t)$ is expressed in terms of the Euler angles $\phi(t), \theta(t), \psi(t)$, which in turn are related to $\mathbf{\Omega} = (\Omega_1, \Omega_2, \Omega_3)$ via the following three differential equations Goldstein (1980),

$$\begin{aligned} \phi_t \sin\theta \sin\psi + \theta_t \cos\psi &= \Omega_1 \\ \phi_t \sin\theta \cos\psi - \theta_t \sin\psi &= \Omega_2 \\ \phi_t \cos\theta + \psi_t &= \Omega_3 \end{aligned}$$

Thus at any time step t, the position of the bacterium is determined by first solving for $\mathbf{v}$ and $\mathbf{\Omega}$ from (2.8) in the local body frame, and then determining the position of the head and flagellum from (2.9) and (2.10) in the laboratory frame. The latter require the Euler angles, which are determined from the above set of differential equations.

3. Results and Discussion

We compared the predicted dimensionless vertical velocity with the SBT calculations of Higdon (1979) as a function of number of turns and the ratio of flagellum radius to the head radius around the geometric parameters of our bot. Recall that Higdon replaces the expression for the stokeslet with a Green's function that consisted of the stokeslet plus a collection of image singularities that ensure the no-slip boundary condition on the head's surface. Our formulation does not include this correction. In addition, we neglect the stokeslets on the small hook that connects the rotor to the helix (Fig. 1A), which were included in the reference calculations from Higdon SBT. We find that our simulation results in the absence of wobble closely match the reference measurements with a maximum error of 15% (Section IV, Supplementary Materials).

Fig. 3B shows a schematic of the bot while highlighting the tilt caused by the asymmetric position of the center of mass of the spherical head. Recall that $\boldsymbol{\ell}'(t)$ is the distance of the center of mass of the head from the center of mass of the helical flagellum. Fig. 3C presents the predicted trajectory when the bot had an equilibrium tilt of 7.6°. The trajectory has two helical paths, one with a small pitch (0.22 mm) and radius (0.01 mm) which is caused by the residual torque exerted by the forces on the rotating flagella about the center of the head, while the second is a result of the asymmetric weight distribution coupled to the counter rotation of the head and has a much larger pitch (8.8 mm) and radius (1.4 mm) - we refer to the latter as the wobble to distinguish it from the smaller helical trajectory. Note that the plot includes an initial transient (up to about $Y = 5$ mm) during which the bot attained a constant vertical orientation about which the bot precessed while translating upwards. Fig. 3D compares the predicted trajectory with the measurements with close agreement between the two. The measurements are represented by dots obtained from each frame, and the spread in the dots indicates the error in determining the center of the head. In addition to the trajectory, the time evolution of the X and Y coordinates of the center of the head also agree well with the predictions. It should be noted that the speed reduced somewhat (due to battery drainage) towards the end of the experiment ($Y > 80$ mm) leading to a small discrepancy at the end (Fig. 3(C-F)). The rotation rate of the head and the flagella was also measured experimentally and compared with the theoretical prediction. During the course

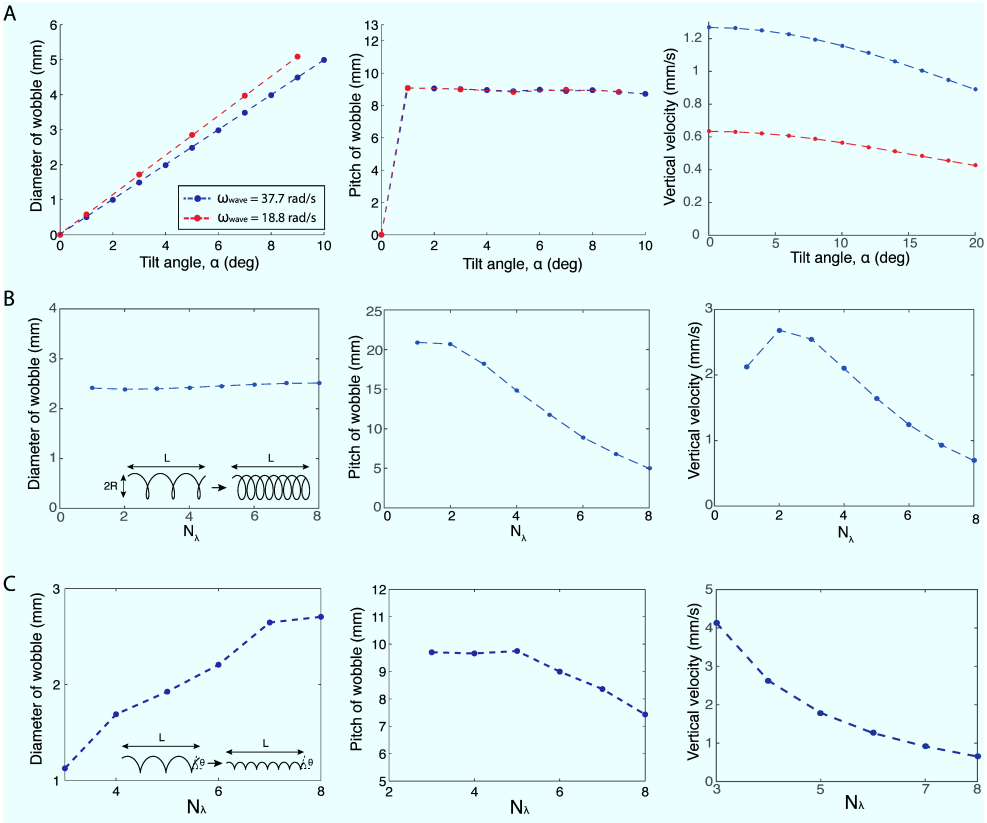

FIGURE 4. The figure plots the radius, pitch and the vertical velocity component for (A) varying tilt angles (α) (B) varying number of helical turns with L and R fixed, and (C) varying number of helical turns with L_c and θ fixed, and therefore L is also fixed.

of this run, $|\Omega_{H,3}|$ was observed to be 0.82 ± 0.16 rad/s, where the standard deviation represents the gradual decrease in magnitude of $\Omega_{H,3}$ due to battery drainage. If we take the instantaneous value of $|\Omega_{H,3}| = 0.75$ rad/s measured when $|\Omega_3| \approx |\omega_{wave}| = 37.7$ rad/s during the experiment, it compares closely with the theoretical prediction for $|\Omega_{H,3}| = 0.84$ rad/s for the same value of ω_{wave} (Table 1). These results show that the slender body theory is able to capture all the salient features of the flow with close quantitative agreement with the experimental measurements. Further, the translation speed with the corrected Green's function and force elements on the hook but without the tilt is 15% higher than that predicted by our code for the same conditions. We therefore conclude that the absence of the these corrections do not significantly alter the conclusions of our study.

Next, we explore the influence of tilt angle and number of helical turns (of the flagellum) on the swimming characteristics of the bot (Fig. 4). To obtain a better physical understanding of the observed trends, we obtain scaling relations from the resistive-force theory of KR, who considered a force-free bacterium with a single flagellum connected to a spherical head, and determined the translational and angular velocities of the head and the flagellum (see appendix). When the contour length of the flagellum ($L_c = L\sqrt{1 + k^2R^2}$) is large compared to R and λ and

$k^2R^2 >> 1$, the translation and angular velocities are of the following order of magnitude ($\alpha = 0$),

$$\frac{v_3}{c} \sim \frac{1}{\left[2 - \left(\frac{3b}{L_c}\right)\ln\left(\frac{ka\sqrt{e}}{4\pi}\right)\right]} \tag{3.1}$$

$$\frac{v_1}{c}, \frac{v_2}{c} \sim \frac{kR^2}{L_c}\frac{1}{\left[1 - \left(\frac{8b}{L_c}\right)\ln\left(\frac{ka\sqrt{e}}{4\pi}\right)\right]} \tag{3.2}$$

$$\frac{\Omega_3}{\omega_{wave}} \sim 1 \tag{3.3}$$

$$\frac{\Omega_{H,3}}{\omega_{wave}} \sim \frac{R^2L_c}{4b^3}\frac{1}{\ln\left(\frac{ka\sqrt{e}}{4\pi}\right)} \tag{3.4}$$

Here, $c = \omega_{wave}/k$ and component 3 of the body-fixed coordinate system is aligned along the axis of the flagellum. The rotating helix results in a helical trajectory even in the absence of tilt, where the radius ($\mathcal{R}$) and the pitch ($\mathcal{P}$) of the resulting helical path in the limit of $k^2R^2 \gg 1$ scale as,

$$\mathcal{R} = \frac{(\mathbf{\Omega} \times \mathbf{v})_\perp}{\Omega_3^2} \sim \frac{v_{1,2}}{\Omega_3} \sim \frac{R^2}{L_c}\frac{1}{\left[1 - \left(\frac{8b}{L_c}\right)\ln\left(\frac{ka\sqrt{e}}{4\pi}\right)\right]}$$

$$\mathcal{P} = \frac{\mathbf{\Omega} \cdot \mathbf{v}}{\Omega_3^2} \sim \frac{v_3}{\Omega_3} \sim \frac{1}{k}\frac{1}{\left[2 - \left(\frac{3b}{L_c}\right)\ln\left(\frac{ka\sqrt{e}}{4\pi}\right)\right]}.$$

Substituting the parameter values for our bot gives the scaling for the radius and pitch of the smaller helical trajectory observed in the simulations (Fig. 4B).

In the presence of the tilt, however, the translation velocity and the angular rotation in the perpendicular direction will have a large contribution from the torque exerted by the offset weight due to which the trajectory of the wobble will be set by the angular velocity of the counter-rotating head. This suggests that there are two time scales in the problem - the first is the inverse of the angular rotation of the flagellum, which determines the smaller helical trajectory and the second is the inverse of the angular rotation of the counter rotating head, which determines the wobble. The calculation of the wobble trajectory requires the translation velocity in the direction perpendicular to the flagellum's axis due to the offset weight, which may be obtained by balancing the torque exerted by the offset weight against the drag on the flagellum ($b^3/L_c^3 \ll 1$ and $k^2R^2 \gg 1$, see appendix),

$$v_{1,2} \sim \frac{\delta mg\Delta kR}{\mu L_c^2}\frac{\ln\left(\frac{ka\sqrt{e}}{4\pi}\right)}{\left[\frac{7}{4} - \left(\frac{2b}{L_c}\right)\ln\left(\frac{ka\sqrt{e}}{4\pi}\right)\right]} \tag{3.5}$$

Since the pitch angle of the smaller helical trajectory is negligible, it may be assumed that the velocity along the axis of the smaller helical path is close to v_3. In that case, the pitch angle of the wobble (γ) is given by,

$$\sin\gamma = \frac{2\pi v_{1,2}}{v_3} \sim \frac{2\pi\delta mg\Delta k^2R}{\mu L_c^2\omega}\ln\left(\frac{ka\sqrt{e}}{4\pi}\right)\frac{\left[2 - \left(\frac{3b}{L_c}\right)\ln\left(\frac{ka\sqrt{e}}{4\pi}\right)\right]}{\left[\frac{7}{4} - \left(\frac{2b}{L_c}\right)\ln\left(\frac{ka\sqrt{e}}{4\pi}\right)\right]}$$

The corresponding radius and pitch of the wobble are ($k^2R^2 \gg 1$),

$$\mathcal{R} \sim \frac{v_{1,2}}{\Omega_H} \sim \frac{4\delta mg\Delta}{\mu\omega_{wave}} \frac{kb^3}{RL_c^3} \frac{\left[\ln\left(\frac{ka\sqrt{e}}{4\pi}\right)\right]^2}{\left[\frac{7}{4} - \left(\frac{2b}{L_c}\right)\ln\left(\frac{ka\sqrt{e}}{4\pi}\right)\right]} \tag{3.6}$$

$$\mathcal{P} \sim \frac{v_3\cos(\gamma)}{\Omega_H} \sim \frac{b^3}{kR^2L_c} \frac{\ln\left(\frac{ka\sqrt{e}}{4\pi}\right)}{\left[2 - \left(\frac{3b}{L_c}\right)\ln\left(\frac{ka\sqrt{e}}{4\pi}\right)\right]}, \tag{3.7}$$

where $\cos\gamma$ is taken to be approximately 1 ($\cos\gamma \approx 0.7$ for our experimental measurements). In the opposite limit of $k^2R^2 \ll 1$, the scaling for radius and pitch of wobble are given by,

$$\mathcal{R} \sim \frac{2\delta mg\Delta}{\mu\omega_{wave}} \frac{kb^3}{RL_c^3} \frac{\left[\ln\left(\frac{ka\sqrt{e}}{4\pi}\right)\right]^2}{\left[-\frac{7}{3} - \left(\frac{2b}{L_c}\right)\ln\left(\frac{ka\sqrt{e}}{4\pi}\right)\right]} \tag{3.8}$$

$$\mathcal{P} \sim \frac{b^3k}{L_c} \frac{\ln\left(\frac{ka\sqrt{e}}{4\pi}\right)}{\left[2 - \left(\frac{3b}{L_c}\right)\ln\left(\frac{ka\sqrt{e}}{4\pi}\right)\right]}, \tag{3.9}$$

Fig. 4A presents the radius, pitch and the vertical velocity of the bot as a function of the tilt angle. With increasing tilt angle, the radius of the wobble increases linearly while decreases with increasing rotation rate (Fig. 4(A1)). The scaling obtained in the limit of $k^2R^2 \gg 1$ broadly reflect this observation since the tilt angle is proportional to Δ although the magnitude of the decrease with rotation rate from simulations is lower than predicted from the scaling arguments. On the other hand, the pitch is independent of both the rotation rate and tilt angle, which is also captured by the simple scaling argument. The vertical velocity is equal to $v_3\cos\gamma$ and is independent of the tilt angle for small tilt angles, in agreement with the simulation results. However, at larger tilt angles, the simulation results deviate from the small tilt approximation, as expected. This is because $\cos\gamma$ gradually decreases as the radius of wobble increases.

Fig. 4B determines the effect of changing the number of turns, $N_\lambda = kL/2\pi$, on the wobble when the radius and the length of the flagellum is kept constant with $R/L_c \ll 1$ in all cases. Under these conditions, increasing the number of turns increases both the contour length and the pitch angle of the helix. The vertical velocity increases linearly with N_λ at small N_λ but decreases at large N_λ due to lower thrust at large pitch angles (Fig. 4(B3)). It should however be noted that the decrease at large N_λ is much steeper than predicted by the RFT since the latter ignores the hydrodynamic interactions between the segments of the helix (Higdon 1979). Increasing the contour length of the helix increases the torque exerted by the rotating helix resulting in an increase of the angular rotation of the counter-rotating head, which in turn reduces the effective rotation rate of the flagellum. Consequently, the pitch of the wobble decreases with increase in the number of turns (Fig. 4(B2)). The diameter of the wobble, however, does not change significantly (Fig. 4(B1)), and this trend is only roughly predicted by the scaling.

The simple scaling also correctly captures the trends with varying N_λ for $k^2R^2 \gg 1$ with constant L_c, L and kR (Fig. 4C). Here, increasing N_λ corresponds to a decreasing R. The decrease in the vertical velocity and the pitch with N_λ occurs for the same reasons detailed above. However, the increase in the diameter of the pitch is explained by the fact that increasing N_λ and therefore decreasing R, reduces the torque exerted by the rotating flagellum, which in turn reduces the angular rotation of the counter rotating head while the transverse velocity due to the torque from the offset weight does not change significantly (Fig. 4(C1)).

These results show that by varying the geometric parameters of the flagellum and on inclusion

L	$6\ \mu$m
N_f	3
k	$3.14\ \mu\text{m}^{-1}$
R	$0.24\ \mu$m
a	$0.045\ \mu$m
b	$2.5\ \mu$m
δm	6×10^{-15} Kg
Δ	$2.5\ \mu$m
ω_{wave}	150 Hz
μ	8×10^{-4} Pa-s (at $30^{\circ}C$)

TABLE 2. Typical parameters for swimming bacteria.

of a small external torque such as that due to gravity, even when the bot is neutrally buoyant, it can lead to large variations in both pitch and diameter of the helical trajectory. It is then interesting to speculate if mass asymmetry could also contribute to the ~~wiggling trajectories~~ wobble observed in bacteria ~~. Since the body of a bacterium head~~ (Darnton *et al.* 2007; Hyon *et al.* 2012). It is well know that the center of mass in nearly spherical biflagellated *Chlamydomonas oligochloris* is located well off the symmetry axis of the cell. Although the cell body rotates approximately around its symmetry axis while it swims, the gravitational torque due to the off-set weight causes a pronounced wobble in the trajectory of the bacteria (Pedley & Kessler 1992), a phenomenon identical to that observed in our bot.

Following on these arguments, the body of a bacterium (such as in *E. coli* or *B. subtilis*) has loosely distributed components such as nucleoid and ribosomes, and hence the mass need not be distributed uniformly in the head. Further, since the density of the bacteria is greater than that of water (1.16 g/cm^3 for *E. coli*) (Godin *et al.* 2007), the bacterium would experience both a net external force and a net external torque during its motion. The translational motion generated by the external force will be small compared to that generated by the thrust of the rotating flagella but the net external torque may be significant enough to cause a large helical trajectory, similar to that observed in the bot. ~~However, more detailed information regarding the head and flagella of bacteria~~ We can estimate the pitch and radius of wobble trajectory for a typical bacteria from the parameters listed in table 2. Note that the buoyant mass of the bacteria is of $O(10^{-15}$ Kg) (Godin *et al.* 2010) while Δ is assumed to be equal to head radius. Substituting these values in the scalings obtained using the resistive force theory for both $kR \ll 1$ and $kR \gg 1$ gives $\mathcal{P} = O(1\ \mu\text{m})$ and ~~careful calculations will be needed to explore this further .~~ $\mathcal{R} = O(0.1\ \mu\text{m})$ suggesting that asymmetry in mass distribution could contribute to wobbles in swimming trajectory. These values are of the same order as those computed for wobble by Hyon *et al.* (2012) due to the off-axis flagellum, $\mathcal{P} = 2.9\ \mu$m and $\mathcal{R} = 0.1\ \mu$m (see their Figure 7) and is close to the lower limit of the range measured by the authors, $\mathcal{P} = 8.9 \pm 6.0\ \mu$m and $\mathcal{R} = 0.91 \pm 0.81\ \mu$m.

While the above calculation assumes the bacteria to be swimming along the gravity direction, wobble will also be observed at all orientation angles other than when the cell is moving exactly perpendicular to the gravity direction. This is because there will always be a component of gravity acting along the flagellar axis that will lead to wobble. Further, the scaling suggests that while pitch is independent of gravity, the radius is proportional to the component of gravity acting along the flagellar axis. Consequently, the radius of the trajectory would vary as the cell orients itself in space with respect to the gravity direction. Under a microscope, an observer will therefore see the projections of the pitch and radius (onto the image plane), which will vary with cell's orientation. Further, we note that any asymmetry of considerable magnitude will result in an overall wobble and multiple sources of asymmetry could increase the observed wobble. We

envision ellipsoidal head and off-axis flagellum to result in further increase in wobble beyond the mechanisms we describe. It will be particularly important in the future to perform calculations accounting for the various sources of asymmetry in the bacterial geometry. These calculations accompanied by detailed experiments of corresponding asymmetries in macroscopic bots will allow us to understand all factors that contribute to wobbling trajectories of a bacterium.

The good agreement between the predictions of SBT and the experiments show that the approximations that lead to SBT formulation, namely, representing the force generated by a rotating filament with a distribution of stokeslets and doublets along center of the flagellum captures closely all details of the flow. Further, our work shows that errors due to the absence of the corrected Green's function for the stokeslets are small. This suggest that the current SBT model is an excellent candidate for investigating collective motion of bacteria compared to the commonly used resistive force theory, which is prone to large errors especially at large cell number densities due to the improper accounting of hydrodynamic interactions.

4. Conclusions

In this study, we have built a working model of a bacterium and observed its detailed motion in a viscous liquid. These details cannot be simultaneously observed for a real bacterium under a microscope. We show that a small asymmetry in the mass distribution in the head can lead to helical trajectories with large pitch and radius, which are reminiscent of the wiggling trajectories observed for swimming bacteria. The detailed motion agrees well with the predictions from slender body theory that accounts for the asymmetric mass distribution in the head. The observed trajectory is comprised of two helical trajectories of different length scales - a large one caused by the asymmetric mass distribution and set by the head rotation rate and a smaller one caused by the rotating flagellum and set by its rotation rate. These results show that small mass asymmetries in real bacteria could lead to large helical trajectories similar to the observed wiggling trajectories in swimming bacteria.

The authors are grateful to Professor Ashok Sangani for providing his SBT code with the modified Green's function, which was used to estimate the magnitude of error in the absence of the correction. Financial support from the Department of Science and Technology, India (SB/S3/CE/089/2013) and Department of Biotechnology, India (BT/PR7712/BRB/10/1229/2013) is acknowledged. MST also acknowledges support from the Swaranajayanti Fellowship (DST/SJF /ETA-01/2010-11).

REFERENCES

Berg, H.C. 2004 *E. coli in Motion*. Springer, New York.

Chwang, A. T. & Wu, T. Y. 1971 A note on the helical movement of micro-organisms. *Proc. R. Soc. B.* **178**, 327.

Cortez, R. 2001 The method of regularized stokeslets. *SIAM J. Sci. Comput.* **23** (4), 1204–1225.

Cortez, R, Fauci, L & Medovikov, A 2005 The method of regularized stokeslets in three dimensions: Analysis, validation, and application to helical swimming. *Phys. Fluids* **031504**.

Darnton, N.C., Turner, L., Rojevsky, S. & Berg, H.C. 2007 On torque and tumbling in swimming *Escherichia coli*. *J. Bacteriol.* **189** (5), 1756–1764.

Dillon, R.H., Fauci, L.J. & Yang, X. 2001 Sperm motility and multiciliary beating: An integrative mechanical model. *Computers & Mathematics with Applications* **23** (4), 1204–1225.

Godin, M., Bryan, A. K., Burg, T. P., Babcock, K. & Manalis, S. R. 2007 Measuring the mass, density, and size of particles and cells using a suspended microchannel resonator. *App Phys Lett* **91** (12), 123121.

Godin, Michel, Delgado, Francisco Feijů, Son, Sungmin, Grover, William H., Bryan, Andrea K., Tzur, Amit, Jorgensen, Paul, Payer, Kris, Grossman, Alan D., Kirschner, Marc W. & Manalis, Scott R. 2010 Using buoyant mass to measure the growth of single cells. *Nat Methods* **7** (5), 387–390.

Goldstein, H. 1980 *Classical mechanics*. *World student series* . Reading (Mass.), Menlo Park (Calif.), Amsterdam: Addison-Wesley.

Gray, J. & Hancock, G. J. 1955 The propulsion of sea-urchin spermatozoa. *J. Exp. Bio* **32** (4), 802–814.

Hancock, G. J. 1953 The self-propulsion of microscopic organisms through liquids. *Proc. R. Soc. A* **217** (1128), 96–121.

Higdon, J. J. L. 1979 The hydrodynamics of flagellar propulsion: helical waves. *J . Fluid Mech.* **94** (2), 331–351.

Hyon, Y., Powers, T.R., Stocker, R. & Fu, H.C. 2012 The wiggling trajectories of bacteria. *J. Fluid Mech.* **705**, 58–76.

Johnson, R.E. 1980 An improved slender-body theory for stokes flow. *J . Fluid Mech.* **99**, 411–421.

Keller, J. B. & Rubinow, S. I. 1976 Swimming of flagellated microorganisms. *Biophys. J.* **16**, 151.

Lauga, E. 2016 Bacterial hydrodynamics. *Annu. Rev. Fluid Mech.* **48**, 105–30.

Lauga, E. & Powers, T. R. 2009 The hydrodynamics of swimming microorganisms. *Rep. Prog. Phys.* **72** (9), 096601.

Lighthill, J. 1976 Flagellar hydrodynamics: The john von neumann lecture. *SIAM Review* **18** (2), 161–230.

Pedley, T. J. & Kessler, J. O. 1992 Hydrodynamic phenomena in suspensions of swimming microorganisms. *Annu. Rev. Fluid Mech.* **24** (24), 313–58.

Phan-Thien, N., Tran-Cong, T. & Ramia, M. 1980 An improved slender-body theory for stokes flow. *J . Fluid Mech.* **99**, 411–421.

Rodenborn, B., Chen, C.-H., Swinney, H. L., Liu, B. & Zhang, H. P. 2013 Propulsion of microorganisms by a helical flagellum. *Proc. Natl. Acad. Sci.* **110** (5), 338–347.

Taylor, G. I. 1952 The action of waving cylindrical tails in propelling microscopic organisms. *Proc. R. Soc. A* **211**, 225–39.

Taylor, G. I. 1967 *Low-Reynolds-number flows. US Natl. Comm. Fluid Mech. Films video.*.

Appendix A. Results from the resistive-force theory of Keller & Rubinow (1976) (KR)

A.1. *Scalings in the absence of tilt from KR*

To obtain approximate scalings for the pitch, radius and vertical component of translation velocity in the presence of the tilt, we utilize the results of KR derived using the resistive force theory, which are strictly applicable in the absence of the tilt. Their analysis predicts all components of velocity and angular rotation of the head and the flagellum (see equations (35)-(39) in KR). These are reproduced below. The velocity component along the axis of the flagellum in the lab-fixed coordinate system is given by,

$$\frac{v_3^{\alpha=0}}{c} = \frac{k^2R^2}{D}\frac{4b^3}{L_c^3}\ln\left(\frac{ka\sqrt{e}}{4\pi}\right) \tag{A 1}$$

where,

$$D = \frac{R^2}{L_c^2}\left[2(1+k^2R^2) - (2+k^2R^2)\left(\frac{3b}{L_c}\right)\ln\left(\frac{ka\sqrt{e}}{4\pi}\right)\right] - \left(\frac{4b^3}{L_c^3}\right)\ln\left(\frac{ka\sqrt{e}}{4\pi}\right)\left[1+2k^2R^2 - (1+k^2R^2)\left(\frac{3b}{L_c}\right)\ln\left(\frac{ka\sqrt{e}}{4\pi}\right)\right],$$

$k = 2\pi/\lambda$ and $c = \omega_{wave}/k$.

The superscript, $\alpha = 0$, emphasizes the absence of tilt. The two perpendicular components are given by,

$$\frac{v_1^{\alpha=0}}{c} = \frac{16}{D}\frac{Rb^3}{L_c^4}\ln\left(\frac{ka\sqrt{e}}{4\pi}\right)\frac{\left(1+k^2R^2\right)^{3/2}(2+\cos\zeta)N}{\left[4+3k^2R^2 - 24(1+k^2R^2)\frac{b}{L_c}\ln\left(\frac{ka\sqrt{e}}{4\pi}\right)\right]}, \text{ and} \tag{A 2}$$

$$\frac{v_2^{\alpha=0}}{c} = \left(\frac{\sin\zeta}{2+\cos\zeta}\right)\frac{V_1^{\alpha=0}}{c} \tag{A 3}$$

where, $\zeta = kL_c\cos\beta$, $\cos\beta = 1/\sqrt{1+k^2R^2}$ and β is the helix angle of the flagellum. The corresponding angular velocities of the head and the tail along the axis of the flagellum are,

$$\frac{\Omega_{3,H}^{\alpha=0}}{\omega_{wave}} = \frac{1}{D}\frac{R^2}{L_c^2}\left[2(1+k^2R^2) - (2+k^2R^2)\left(\frac{3b}{L_c}\right)\ln\left(\frac{ka\sqrt{e}}{4\pi}\right)\right] \tag{A 4}$$

$$\frac{\Omega_3^{\alpha=0}}{\omega_{wave}} = \frac{1}{D}\left(\frac{4b^3}{L_c^3}\right)\ln\left(\frac{ka\sqrt{e}}{4\pi}\right)\left[1+2k^2R^2 - (1+k^2R^2)\left(\frac{3b}{L_c}\right)\ln\left(\frac{ka\sqrt{e}}{4\pi}\right)\right] \tag{A 5}$$

A.2. *Scaling for transverse velocity in the presence of tilt*

In order to obtain the approximate scaling for the transverse velocity induced by the off-set weight, we start with the angular momentum balance in the transverse direction obtained by KR (4th of equation (34) in KR) and introduce on the right hand side, the approximate expression for the torque due to the off-set weight,

$$-\cos\beta\left(1-\frac{k^2R^2}{4}\cos^2\beta\right)v_2 + \frac{R}{L_c}\cos^2\beta\sin\zeta v_3 + \frac{2}{3}\cos^2\beta\left(1-\frac{k^2R^2}{4}\cos^2\beta\right)\Omega_1 L_c - \frac{R\sin\zeta}{kL_c^2}(2-k^2R^2\cos^2\beta)\Omega_3 L_c \sim \frac{\delta mg\Delta}{2\pi\mu L_c^2}\ln\left(\frac{ka\sqrt{e}}{4\pi}\right) \tag{A 6}$$

The momentum balance equation in the same transverse direction is given by (2nd of equation (34)),

$$\left[2-\frac{k^2R^2}{2}\cos^2\beta-3\frac{b}{L}\ln\left(\frac{ka\sqrt{e}}{4\pi}\right)\right]v_2-\frac{R}{L_c}\cos\beta\sin\zeta v_3-\cos\beta\left(1-\frac{k^2R^2}{4}\cos^2\beta\right)\Omega_1 L_c + \frac{R}{\zeta L_c}(2-k^2R^2\cos^2\beta)\sin\zeta\Omega_3 L_c = 0 \quad \text{(A 7)}$$

Since we expect the transverse velocity during a wobble to be dominated by the torque exerted by the off-set weight, we drop the terms involving v_3 and Ω_3 while eliminating Ω_1 from the above two equations,

$$v_2 \sim \frac{\delta mg\Delta\sqrt{1+k^2R^2}}{\mu L_c^2}\frac{\ln\left(\frac{ka\sqrt{e}}{4\pi}\right)}{\left[-\frac{7}{3}\left(1-\frac{k^2R^2}{4(1+k^2R^2)}\right)+\frac{2b}{L_c}\ln\left(\frac{ka\sqrt{e}}{4\pi}\right)\right]} \quad \text{(A 8)}$$

The velocity in the other transverse direction (v_1) is also of the same order of magnitude.